Sn-Doped Carbon Black as an Active Conductive Additive for Lithium-Ion Batteries

Hyeonsu Yang,[a, b] Seonghee Kim,[a] Jun Kang,*[c, d] and Oi Lun Li*[a]

Carbon black is commonly used as a conductive additive for lithium-ion battery (LIB) electrodes owing to its high electrical conductivity and cost-effectiveness. However, the role of traditional conductive additives has been limited to imparting conductivity to the electrode. In this study, we investigate the effect of incorporating Sn nanoparticles, which form an alloy with lithium, into a conductive carbon matrix (Sn@C) for enhancing the lithium storage capacity. This approach combines an active material with a conductive additive and successfully demonstrates the utilization of Sn@C as an "active" conductive additive for LIBs. Sn@C is synthesized via plasma engineering, wherein Sn nanoparticles are uniformly dispersed within a carbon matrix. When Sn@C-500, Sn@C annealed at 500 °C, is used as an "active" conductive additive in LIB half-cell with a graphite anode, ~10 % higher reversible capacity than that of a commercial conductive additive (Super P) is achieved. Further, electrochemical impedance spectroscopy studies reveal that Sn@C-500 exhibits a lower internal resistance than Super P, confirming its effectivity in providing internal conductivity to the electrode. Our results open up the possibilities for improving the performance of graphite anodes in LIBs using Sn-doped carbon as an active material and conductive additive.

Introduction

Lithium-ion batteries (LIBs) have revolutionized portable electronics and played a pivotal role in electrifying transportation.[1,2] The increasing demand for high-performance LIBs with higher capacities and faster charging capabilities has propelled the development of new materials and technologies.[3] The performance of LIBs primarily depends on the selection of active materials and optimization of electrode formulations.[4,5] The conductive additive is a crucial component in electrode manufacturing and plays a pivotal role in enhancing the electrical conductivity of electrodes and facilitating charge transfer.[6,7] Therefore, appropriate utilization of conductive additives is essential to maximize the potential performance of the anode material.

Carbon black (CB), a cost-effective carbonaceous material, is commonly used as a conducting additive in battery electrodes due to its high electrical conductivity.[8,9] However, CB exhibits low Li storage capacity, restricting its role to a conductive agent in the electrode.[10–12] Therefore, the quantity of conductive additives in a cell should be minimized while maintaining its conductivity to optimize its energy density and specific capacity.[13,14] For instance, automobile industries integrate high-capacity materials, such as Si, into the graphite anode of LIBs to enhance the reversible capacity of the batteries.[15,16] In the case of the Tesla Model 3, it incorporates 5–10 % of Si in its anode.[17] However, adding such materials beyond a specific ratio can lead to reduced electrode conductivity and lifespan owing to the volume expansion of materials.[18–20] Therefore, additional conductive materials are required to compensate for the decreased conductivity. Hence, enhancing the cell capacity by introducing nonconductive materials results in a trade-off, necessitating the addition of conductive materials, decreasing the energy density.

Sn is a promising active material owing to its high theoretical capacity (994 mAh g^{-1}) and excellent Li-ion diffusion properties, rendering it an attractive candidate for improving the energy storage capabilities of LIBs.[21,22] Moreover, metallic Sn exhibits inherently high electrical conductivity and offers additional advantages, including wide availability and low cost.[23,24] Theoretically, Sn can be applied as a conductive and active material for high Li storage capacity, which can remarkably enhance the performance of graphite anodes in LIBs.

However, Sn undergoes considerable volume expansion during charge/discharge cycles, leading to electrode degradation and reduced cycling stability.[25,26] Extensive research has been conducted to address these issues, wherein incorporating

[a] H. Yang, Dr. S. Kim, Prof. O. Lun Li
    Department of Materials Science and Engineering,
    Pusan National University, 2 Busandaehak-ro 63beon-gil, Geumjeong-gu,
    Busan 46241, Republic of Korea
    E-mail: helenali@pusan.ac.kr

[b] H. Yang
    Interdisciplinary Graduate School of Engineering Sciences,
    Kyushu University, 6-1 Kasuga-Koen Kasuga-shi Fukuoka 816-8580, Japan

[c] Prof. J. Kang
    Division of Marine System Engineering,
    Korea Maritime and Ocean University, 727, Taejong-ro, Yeongdo-gu, Busan
    49112, Republic of Korea
    E-mail: junkang@kmou.ac.kr

[d] Prof. J. Kang
    Interdisciplinary Major of Maritime AI Convergence,
    Korea Maritime and Ocean University, 727, Taejong-ro, Yeongdo-gu, Busan
    49112, Republic of Korea

Batteries & Supercaps

Research Article
doi.org/10.1002/batt.202400294

Chemistry
Europe
European Chemical
Societies Publishing

nano-sized Sn particles into carbon materials emerges as the most effective strategy.[27–31] Sn nanoparticles alleviate the mechanical stress during cycling and shorten the pathways for electron and Li$^+$ transport,[32,33] whereas the CB structure prevents the damage caused by the volume expansion of Sn, thus improving the electrical conductivity of the cell.[34–37]

In this study, the Sn-carbon composite (Sn@C) conductive additive was synthesized via plasma engineering. Plasma engineering follows a simple bottom-up synthesis approach that directly incorporates Sn nanoparticles into the carbon structure using a toluene solution and Sn electrode as the carbon and Sn precursors, respectively (Figure 1). We utilized the inherent conductivity of Sn that can form an alloy with Li, to enhance the Li storage capacity and investigated its influence on the electrochemical performance of LIB anodes. Traditional conductive additives primarily impart conductivity to the material; however, in this study, we demonstrate that Sn@C acts as an active conductive additive that enhances the cycling stability and rate capability of LIBs.

Results and Discussion

As detailed in the supporting information, Sn@C was synthesized using the plasma-in-liquid technique (Figure S1). Plasma engineering involves applying a high pulse voltage to aromatic organic precursors, resulting in liquid breakdown and the generation of various active species such as H, C$_2$, and CH in the plasma region. These radicals undergo further dissociation and recombination steps, ultimately leading to direct polymerization to form carbon nanoparticles.[38] The samples were denoted as Sn@C-Raw, Sn@C-500, and Sn@C-1000, corresponding to the annealing temperatures.

The morphology and microstructure of the synthesized materials were determined using TEM (Figure 2(a–c)) and HR-TEM (Figure 2(d–f)). The synthesized carbon matrix exhibits a similar morphology to that of typical CB, with sizes ranging from approximately 20 to 40 nm. These particles are interconnected, forming mesopores and macropores.

The presence of these mesopores and macropores mitigates the electrode damage due to the volume expansion of Sn

during the alloying/dealloying of Sn particles with Li.[39] Lattice fringe spacings of 0.291 nm in the HR-TEM image of Sn@C-Raw (Figure 2d and S2) correspond to the (200) planes of metallic Sn.[40] Further, the size of the Sn particles increases with the annealing temperature due to particle coalescence. Figure 2(a) and (d) reveal that the Sn particles in Sn@C-Raw are uniformly dispersed throughout the material and exhibit sizes of approximately 4–8 nm. The thermal treatment of Sn particles causes agglomeration, which increases their size to approximately 20 nm in Sn@C-500 (Figure 2(b) and (e)). Sn@C-1000 (Figure 2(c) and 2(f)) exhibits larger-sized Sn particles of (20–30 nm) than Sn@C-500.

The HR-TEM images (Figure 2(d–f)) reveal that the carbon particles in Sn@C exhibit a predominantly disordered amorphous structure, which could be attributed to the synthesis method used in this study, wherein carbon particles are heated at high temperatures via a plasma process and rapidly cooled in a solution at lower temperatures.[41,42] The disordered structure of the material enhances Li$^+$ intercalation by creating additional pathways for Li storage, thus improving the dynamic performance.[43] Additionally, the EDS mapping results (Figure 2(g)) confirm the uniform dispersion of Sn particles within the carbon matrix.

Figure 3(a) presents the XRD patterns of all three types of Sn@C samples, which display a distinct Sn peak regardless of the annealing temperature, indicating the successful incorporation of Sn in the synthesized material. However, the carbon peak is indistinguishable owing to the intense Sn peak. Hence, XRD analysis of the carbon material synthesized without the Sn precursor was performed and is given in Figure S3, showing broad (002) and (100) planes with a gradual slope, indicating an amorphous carbon structure. Raman spectra of Sn@C-Raw, Sn@C-500, and Sn@C-1000 given in Figure 3(b) exhibit the characteristic peaks for disordered (D band) and graphitic carbon (G band). The I_D/I_G ratios for Sn@C-Raw, Sn@C-500, and Sn@C-1000 are 0.94, 0.98, and 1.03, respectively, suggesting that the fraction of amorphous Sn@C increases with annealing temperatures, which agrees with the previous findings obtained using the same synthesis method.[44]

Figure 3(c) shows the TGA results for Sn@C-500. The TGA curve of Sn@C-500 exhibits minimal changes up to 220 °C approximately. A marginal mass increase is observed over the approximate temperature range of 220–400 °C, which could be attributed to the oxidation of Sn, whereas a substantial weight loss occurs from approximately 400–580 °C indicating the carbon decomposition. Figure S4(a) and (b) show the TGA curves for Sn@C-Raw and Sn@C-1000, respectively, exhibiting similar trends. Assuming that the heating of Sn@C results in the SnO$_2$ formation during TGA, the Sn concentration in an Sn@C sample can be calculated using equation (1) as follows:[45]

$$Sn(wt.\%) = 100 \times \frac{molecular\ weight\ of\ Sn}{molecular\ weight\ of\ SnO_2} \times \frac{final\ weight\ of\ SnO_2}{initial\ weight\ of\ Sn@C} \quad (1)$$
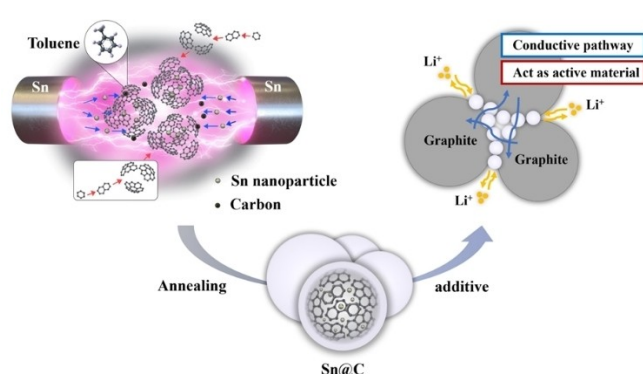

Figure 1. Schematic of the Sn@C synthesis and its role as an active conductive additive.
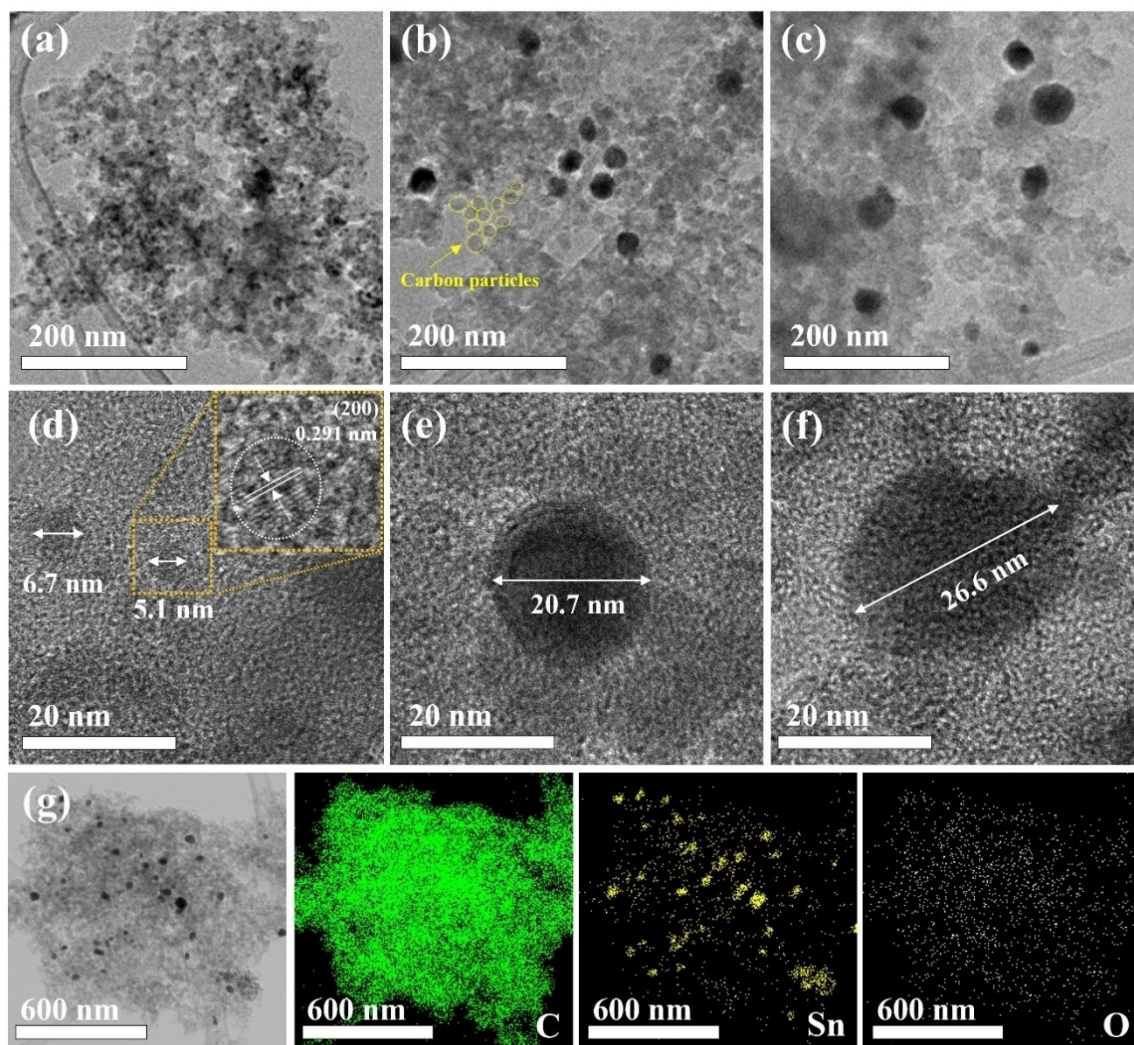
Figure 2. TEM images of (a) Sn@C-Raw, (b) Sn@C-500, and (c) Sn@C-100; HR-TEM images of (d) Sn@C-Raw, (e) Sn@C-500, and (f) Sn@C-1000; and (g) EDS mapping of Sn@C-500.

Therefore, the Sn concentrations in Sn@C-Raw, Sn@C-500, and Sn@C-1000 are calculated to be 25.68, 22.06, and 18.51 wt.%, respectively.

The surface chemical composition of Sn@C-500 was evaluated via XPS. The XPS spectrum of Sn@C-500 (Figure 3(d)) exhibits peaks corresponding to Sn, C, and O.

The presence of O could be attributed to the surface oxidation of Sn during the XPS analysis. Figure 3(e) reveals that the Sn 3d spectrum exhibits two characteristic peaks at 487.2 and 495.5 eV, corresponding to the binding energies of Sn $3d_{5/2}$ and Sn $3d_{3/2}$, respectively, confirming the presence of Sn^{4+} in the as-prepared composite owing to the oxidation of Sn to SnO_2 on the Sn@C-500 surface under ambient conditions. However, the XRD results reveal that a majority of Sn particles remain in the metallic state, which could be ascribed to the surface oxidation of Sn, as reported previously in the literature.[46] The high-resolution C 1s XPS spectrum reveals three peaks at 284.6, 285.4, and 288.8 eV, representing the C—C, C—O, and O=C—O bonds, respectively (Figure 3(f)). Figure S5

shows the high-resolution O 1s XPS spectrum of Sn@C-500, exhibiting a peak at approximately 532 eV corresponding to the Sn—O bond, indicating the oxidation of Sn to SnO_x on the material surface.

The N_2 adsorption–desorption isotherms of Sn@C-500, Sn@C-Raw, and Sn@C-1000 are shown in Figure 4(a), S6(a), and S6(c), respectively. The surface area, total pore volume, and average pore size of each material are presented in Table 1. Immediately after synthesis, Sn@C-Raw exhibits a specific surface area of 172.3 $m^2 g^{-1}$, which remarkably increases to 232.9 and 234.1 $m^2 g^{-1}$ after thermal treatment at 500 and 1000 °C, respectively. Additionally, the total pore volume of the annealed samples is marginally higher than that of the raw sample, which could be attributed to the agglomeration and relocation of small-sized Sn particles (4–8 nm), as observed in the TEM images, leading to the formation of pores within the carbon matrix. The pore-size distribution of Sn@C composites is given in Figure 4(b), S6(b), and S6(d). The pore size of Sn@C-500 ranges from 10 to 110 nm, indicating the presence of abundant
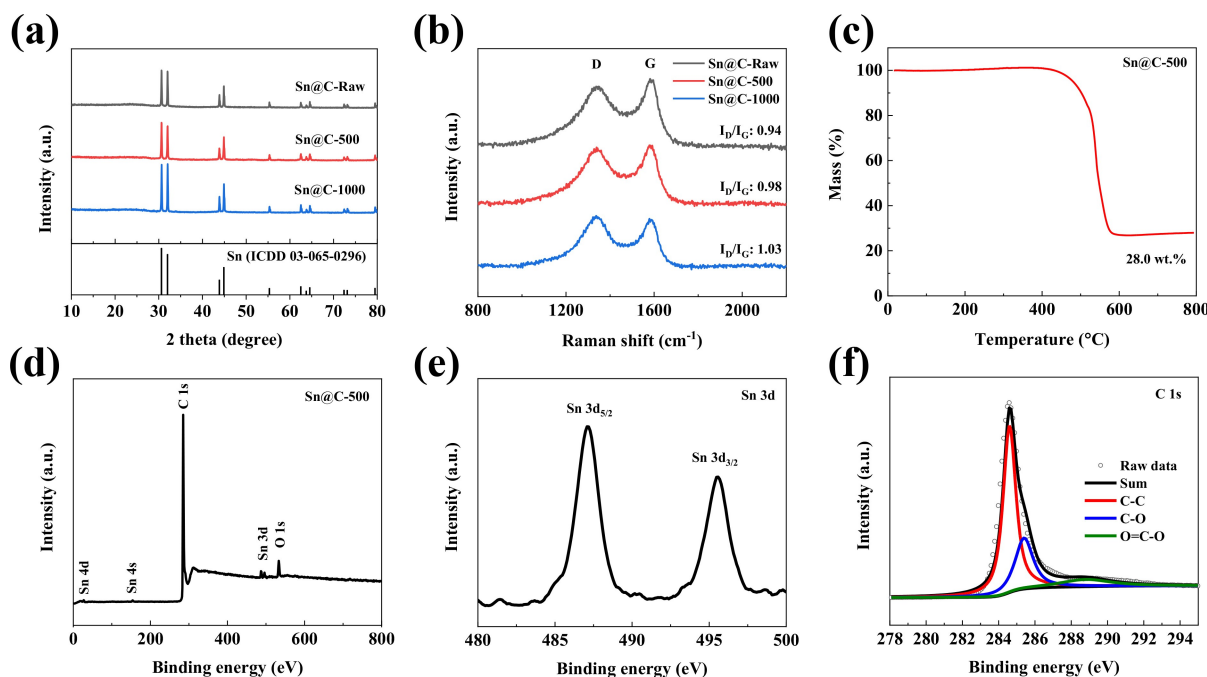
Batteries & Supercaps

Research Article
doi.org/10.1002/batt.202400294

Chemistry Europe
European Chemical
Societies Publishing

Figure 3. (a) XRD patterns and (b) Raman spectra of Sn@C-Raw, Sn@C-500, and Sn@C-1000; (c) TGA curve of Sn@C-500; (d) Wide XPS spectra of Sn@C-500; High-resolution XPS spectra of (e) Sn 3d, and (f) C 1s peaks.
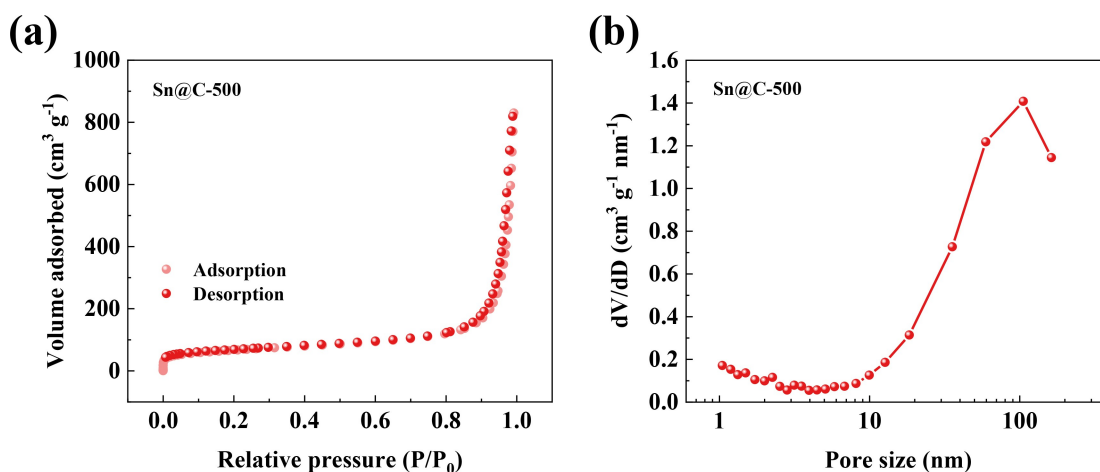

Figure 4. (a) N$_2$ adsorption–desorption isotherm and (b) BJH pore-size distribution of Sn@C-500.

macropores and mesopores, which is consistent with the TEM and HR-TEM findings.

Table 1. BET surface area, total pore volume, and average pore size of Sn@C and Super P.

Material	BET Surface area (m^2 g^{-1})	Total pore volume (cm^3 g^{-1})	Average pore size (nm)
Sn@C-Raw	172.3	1.0626	24.665
Sn@C-500	232.9	1.2161	20.887
Sn@C-1000	234.1	1.1644	19.896
Super P	55.6	0.2191	15.741

These large and small pores facilitate rapid Li-ion exchange and provide inner pore space to accommodate the Sn expansion during cycling, enhancing material stability.[39,47–49]

Figure 5(a) shows the CV curves of Sn@C-500 in the first three cycles within a potential range of 0.01–3.0 V (vs. Li$^+$/Li) and a scanning rate of 0.1 mV s^{-1}. A cathodic peak appears gradually at approximately 0.59 V in the first cycle, which disappears in subsequent cycles owing to the formation of a solid electrolyte interface (SEI) on the surface of the active material. Continuous anodic peaks are observed at 0.59, 0.72, and 0.79 V, indicating the reaction of Sn with lithium and its contribution to the Li storage capacity. However, these peaks weaken from the second cycle onwards. The close resemblance between the second and third scan profiles suggests excellent
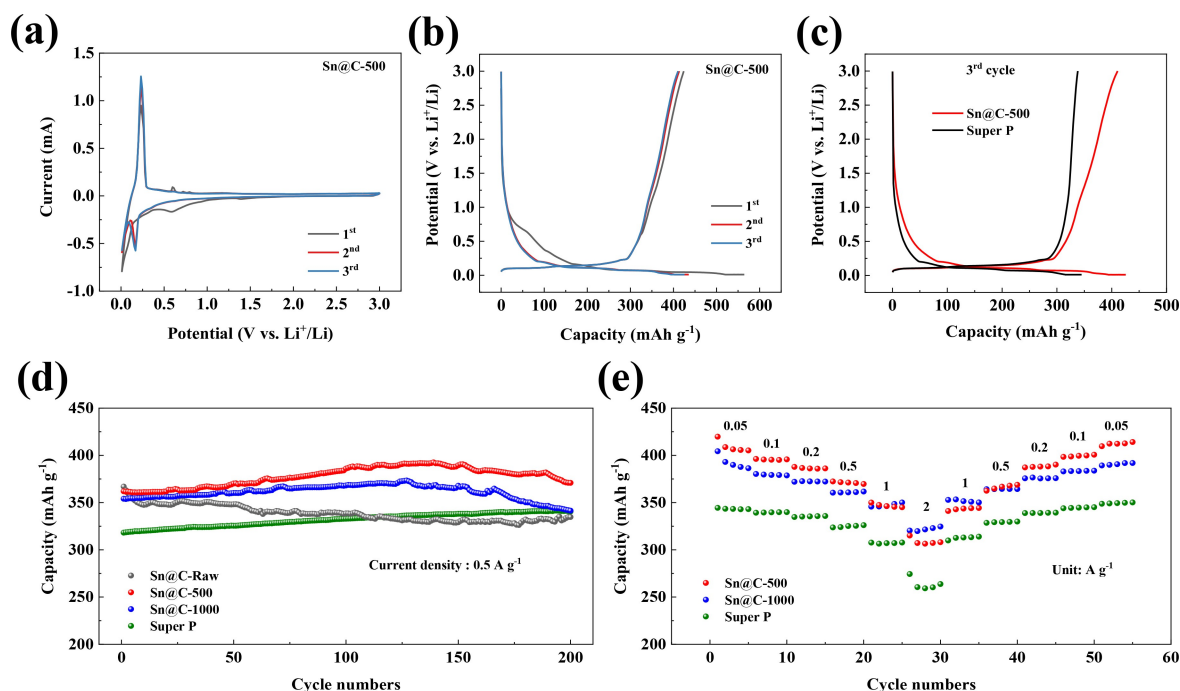
Figure 5. (a) CV curves of Sn@C-500 in a voltage range of 0.01–3 V (vs. Li$^+$/Li) at a scan rate of 0.1 mVs^{-1}; (b) Galvanostatic charge/discharge curves of Sn@C-500 during the initial three cycles at 0.05 Ag^{-1}; (c) Charge/discharge curves of Sn@C-500 and Super P carbon black in the 3rd cycle; (d) Cycling performances of Sn@C-Raw, Sn@C-500, Sn@C-1000, and Super P at 0.5 Ag^{-1} current density; and (e) Rate capability performances of Sn@C-500, Sn@C-1000, and Super P at various current densities ranging from 0.05 to 2 Ag^{-1}.

electrochemical reversibility of the electrode because Sn@C-500 is used as a conductive additive, resulting in a lower proportion of Sn throughout the entire electrode. To investigate the reversible reaction of Sn included in the material, we recorded the CV curve of the cell assembled using Sn@C-500 as the active material (Figure S7).

The volume expansion due to increased Sn content within the electrode results in a considerable peak corresponding to the SEI layer formation. However, even after the second cycle, Sn-related anodic peaks are continuously observed at 0.59, 0.72, and 0.79 V, confirming that the Sn included in the material enhances the reversible capacity. In contrast, the CV curve of Sn@C-Raw (Figure S8(a)) exhibits broad and irreversible oxidation peaks ascribed to the volume expansion of Sn owing to its relatively high content, as observed during the TG analysis. The CV curve of Sn@C-1000 (Figure S8(b)) is similar to that of Sn@C-500. In contrast, the CV curves of Super P used as the reference electrode (Figure S8(c)) demonstrate only cathodic peaks at approximately 0.55 V, which could be attributed to SEI formation and are not related to Sn.

Figure 5(b) shows the galvanostatic charge/discharge curve of Sn@C-500 during the first three cycles. In the first cycle, a gradual region is formed from approximately 0.9 to 0.4 V, attributed to electrolyte decomposition, followed by a slow voltage decrease till 0.01 V; thereafter, a gradual capacity increase is observed from 0.5 to 3.0 V. The second cycle shows a highly reversible charge/discharge capacity, emulating the behavior of a material containing hard carbon. These results are consistent with the CV results. Therefore, the appropriate

utilization of graphite and hard carbon anodes enhances the performance of Li-ion battery electrodes.[50–55]

Comparing the charge/discharge curves of Sn@C-500 and Super P in the third cycle (Figure 5(c)) reveals that Sn@C-500 exhibits considerable capacity enhancements within the voltage range of 0.4–3.0 V, surpassing the performance of Super P. These improvements could be attributed to the surface adsorption of Li ions onto Sn@C, which is a characteristic Li-ion storage mechanism associated with hard carbon.

To evaluate the gravimetric energy density (GED) of Sn@C-500, we used a simplified method to estimate the GED when a graphite anode with Sn@C-500 conductive additive is coupled with NCM811, as shown in following equation (2):[56,57]

$$E_g = k \Delta U \frac{C_p C_n}{C_p + C_n} \qquad (2)$$

where E_g represents the GED of the full cell, k denotes the fraction of active material, ΔU is the average voltage difference between the cathode (NCM811 with an average voltage of 3.95 V vs. Li$^+$/Li and a specific capacity of 185 mAhg^{-1}) and the anode, and C_p and C_n indicate the specific capacities of the cathode and anode, respectively. When the NCM811||graphite/Super P system is normalized to 1.0, the NCM811||graphite/Sn@C-500 system is normalized to 1.004, indicating that almost the same GED can be achieved when using Sn@C-500 to replace the Super P conductive additive.

The Raman spectra infer that the enhanced capacity could be ascribed to the disordered nature of Sn@C-500, coupled

with the capacity increase due to surface adsorption facilitated by its large surface area (232.9 m^{2}g^{-1}).

Additionally, the results confirm a complex reversible reaction of Sn, as indicated by the CV results. The Sn@C structure acts as a conductive additive and enhances the Li-ion storage capability of the anode material.

Figure S9 shows the first cycle charge/discharge curves and initial Coulombic efficiencies (ICE) of Sn@C-Raw, Sn@C-500, Sn@C-1000, and Super P at a current density of 0.05 Ag^{-1}. The Sn@C-Raw electrode exhibits the highest discharge capacity of 440.7 mAhg^{-1} and a lower ICE of 67.8% owing to the formation of a thick SEI layer, consistent with the CV results. In contrast, Sn@C-500 and Sn@C-1000 exhibit high discharge capacities of 423.8 and 396.0 mAhg^{-1}, with relatively higher ICE values of 75.1 and 74.5%, respectively. Although the ICE values are lower than that of Super P (82.8%), the Sn@C samples remarkably outperform Super P in terms of discharge capacity (338.5 mAhg^{-1}). The lower ICE of Sn@C than that of Super P could be attributed to the hard carbon property of the material and the volume expansion of Sn, as confirmed by the TEM images, XRD patterns, and Raman spectra. However, we had previously succeeded in enhancing the ICE by doping lithium into the pure carbon material using the synthesis method employed in this study.[58] Therefore, the ICE can be enhanced by synthesizing the Sn@C composite material and doping it with lithium in future studies.

To assess the applicability of Sn@C as an "active" conductive additive, the cycling performances of Sn@C-Raw, Sn@C-500, and Sn@C-1000 were compared to those of Super P, as shown in Figure 5(d). Sn@C-500 exhibits the highest reversible capacity and lifespan, maintaining a reversible capacity of 375 mAhg^{-1} over 200 cycles. This reversible capacity is ~10% higher than that of Super P (335 mAhg^{-1}). Further, Sn@C-1000 demonstrates excellent reversible capacity; however, it decreases after ~150 cycles due to the volume expansion of large Sn particles, as observed in the TEM images. Moreover, Sn@C-Raw exhibits a rapid decline in anode performance as the number of cycles increases, ascribed to its relatively high Sn content and low electrical conductivity due to the absence of heat treatment.

The specific capacity of Sn@C-500, when the conductive additive is included in the calculation of capacity, is also evaluated at a current density of 0.5 Ag^{-1} and presented in Figure S10. Sn@C-500 maintained a reversible capacity of over 310 mAhg^{-1} for 50 cycles. This is approximately 30 mAhg^{-1} higher than when using Super P (280 mAhg^{-1}).

Rate capability tests were conducted to evaluate the stabilities of Sn@C-500, Sn@C-1000, and Super P as conductive additives, and the results are given in Figure 5(e). The test involves a gradually increasing the current density from 0.05 to 2 Ag^{-1} and then reverting to 0.05 Ag^{-1}. The anode incorporated with Sn@C-500 exhibits high discharge capacities of 406.4, 395.4, 387.8, 372.4, 350.0, and 307.2 mAhg^{-1} at current densities of 0.05, 0.1, 0.2, 0.5, 1, and 2 Ag^{-1}, respectively, indicating that Sn@C-500 enhances the reversible capacity of the anode and acts as a conductive additive, even at high current densities. At a high current density of 2 Ag^{-1}, Sn@C-500 exhibits a marginally lower reversible capacity than that of Sn@C-1000 but outperforms Super P (270.2 mAhg^{-1}). Additionally, when the current density is reverted to 0.05 Ag^{-1}, the original capacity is stably restored, indicating that the material can withstand variable current densities while maintaining high stability. However, Figure S11 shows that the performance of Sn@C-Raw degrades remarkably at high current densities owing to its low conductivity. Hence, incorporating Sn provides extra conductivity and improves the Li-ion storage capacity of the anode. However, adequate annealing treatment is required to ensure efficient conductivity of the carbon matrix while minimizing the agglomeration of Sn particles.

EIS was performed to comprehensively analyze the conductivities and Li-ion diffusion behaviors in the anode. The EIS test was conducted during the 1st and 50th cycles. The Nyquist plots and fitted data are shown in Figure 6(a, b), and Table 2, respectively.

An EIS curve comprises a depressed semicircle in the high-frequency and intermediate-frequency ranges and a sloping line in the low-frequency range. The semicircle corresponds to the charge transfer resistance (R_{CT}) and migration resistance of Li ions through the SEI layer (R_{SEI}), whereas the slope of the line reflects the diffusion Warburg impedance (W_0) of Li ions within the electrode material.[31,59] Figure S12 shows the equivalent circuit used for fitting. R_S and R_{CT} are the electrolytic and charge transfer resistances, respectively. R is the resistance ascribed to
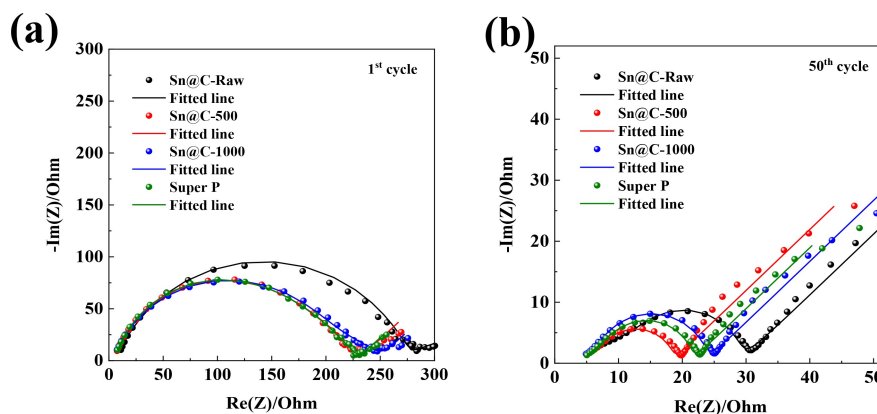

Figure 6. Nyquist plots of (a) the 1st and (b) the 50th cycles of Sn@C-Raw, Sn@C-500, Sn@C-1000, and Super P.

Batteries & Supercaps

Research Article
doi.org/10.1002/batt.202400294

Chemistry Europe
European Chemical
Societies Publishing

Table 2. Comparison of the impedance of Sn@C-Raw, Sn@C-500, Sn@C-1000 and Super P at their 1st and 50th cycles.

Material	1st cycle		50th cycle	
	R_S ($\Omega\,cm^{-2}$)	R ($\Omega\,cm^{-2}$)	R_S ($\Omega\,cm^{-2}$)	R ($\Omega\,cm^{-2}$)
Sn@C-Raw	6.325	293.86	3.93	25.01
Sn@C-500	3.76	223.93	4.31	13.78
Sn@C-1000	3.75	244.24	3.40	19.97
Super P	3.80	224.41	4.24	16.87

the combined effect of Li-ion movement through the SEI layer and charge transfer. CPE$_1$ and CPE$_2$ represent the electric double-layer capacitances. The corresponding fitting values for R_S and R are listed in Table 2. As shown in Figure 6(a), Sn@C-500 and Sn@C-1000 display R values of 223.93 and 244.24 Ω, respectively, during the first cycle. The values are comparable to that of Super P (224.41 Ω). Sn@C-Raw exhibits the highest R-value of 293.86 Ω, indicating insufficient conductivity and poor electrochemical performance due to the absence of thermal treatment. Figure 6(b) shows that after 50 cycles, Sn@C-500 exhibits the lowest R-value (13.78 Ω) among the tested samples, even lower than that of Super P (16.87 Ω), suggesting that the Sn@C-500 additive ensures optimal contact between the electrolyte and electrode throughout the cycling process. This enhanced contact, facilitated by improved conductivity and faster charge transfer dynamics, contributes to the superior electrochemical performance demonstrated. Moreover, the impedance of the Sn@C-500 electrode after cycling is smaller than that of the electrode before cycling, confirming that it possesses faster charge transfer after cycling. The EIS analyses demonstrate that the Sn@C-500 shortens the diffusion path of lithium ions.

To examine the role of Sn in imparting conductivity to the electrode, carbon material without Sn was synthesized, and EIS measurement was performed (Figure S13). The R-value of the carbon material without Sn (59.81 Ω) is remarkably higher than that of Sn@C-500 (13.78 Ω). Further, this high R-value exceeds twice the highest value in Sn@C samples, which is 25.21 Ω for Sn@C-Raw. Therefore, Sn contained in Sn@C contributes remarkably to securing the conductivity within the electrode, ensuring effective charge transfer.

The structural stability of the electrode during cycling was investigated by analyzing the surface morphology of the Sn@C-500 anode via SEM before cycling, after 100 cycles, and after 200 cycles (Figure S14 (a–c)). The overall structure of Sn@C-500 is preserved without considerable cracking or particle expansion after 100 and 200 cycles. This indicates that the network structure formed by the graphite electrode and Sn@C-500 plays a crucial role in suppressing the volume expansion of Sn during electrochemical cycling.

Conclusions

In this study, we successfully synthesized Sn@C as an active conductive additive via plasma engineering. The as-synthesized Sn@C exhibited similar physical properties to that of carbon black (CB), and their particle sizes ranged from 20 to 40 nm. Sn was encapsulated within the amorphous hard carbon structure. The as-synthesized Sn@C was annealed at various temperatures and utilized as a conductive additive for Li-ion battery anodes. A comparison of their electrochemical performances with those of a commercial conductive additive, Super P carbon black, revealed that Sn@C-500 showed a reversible capacity of 370.88 mAh g^{-1} after the 200th cycle at a current density of 0.5 A g^{-1}, which was 8.6% higher than that of Super P (341.44 mAh g^{-1}). The enhanced reversible capacity was attributed to the presence of Sn nanoparticles in the carbon matrix and the morphology of the hard carbon, which improved the Li storage capabilities of Sn@C-500. Additionally, Sn@C-500 demonstrated a reversible capacity of 307.23 mAh g^{-1} at a relatively high current density of 2 A g^{-1}, which exceeded that of Super P (260.52 mAh g^{-1}) by over 18%. EIS measurements revealed that Sn@C-500 had the lowest internal impedance after 50 cycles, indicating that the material effectively improved the conductivity of the electrode as a conductive additive. Further, the SEM images of the electrode obtained before and after the cycles confirmed the structural integrity of the electrode after 200 cycles, demonstrating a highly stable synergy between the active material and conductive additives. Therefore, our results offer valuable insights into using Sn-doped carbon as "active" conductive additives to enhance the performance of Li-ion battery anodes, which opens up the possibilities of developing advanced battery materials in the future.

Supporting Information

Experimental details and further figures are provided.

Conflict of Interests

The authors declare no conflict of interest.

Data Availability Statement

The data that support the findings of this study are available on request from the corresponding author. The data are not publicly available due to privacy or ethical restrictions.

[1] G. Harper, R. Sommerville, E. Kendrick, L. Driscoll, P. Slater, R. Stolkin, A. Walton, P. Christensen, O. Heidrich, S. Lambert, A. Abbott, K. Ryder, L. Gaines, P. Anderson, *Nature* **2019**, *575*, 75–86.

[2] N. Nitta, F. Wu, J. T. Lee, G. Yushin, *Mater. Today* **2015**, *18*, 252–264.

[3] M. Armand, J.-M. Tarascon, *Nature* **2008**, *451*, 652–657.

[4] P. Zhu, P. R. Slater, E. Kendrick, *Mater. Des.* **2022**, 111208.

[5] J.-M. Cao, K.-Y. Zhang, J.-L. Yang, Z.-Y. Gu, X.-L. Wu, *Chin. Chem. Lett.* **2024**, *35*, 109304.

[6] H. Li, Z. Wang, L. Chen, X. Huang, *Adv. Mater.* **2009**, *21*, 4593–4607.

[7] H. Hou, X. Qiu, W. Wei, Y. Zhang, X. Ji, *Adv. Energy Mater.* **2017**, *7*, 1602898.

[8] M. E. Spahr, D. Goers, A. Leone, S. Stallone, E. Grivei, *J. Power Sources* **2011**, *196*, 3404–3413.

[9] Y. Fan, G. D. Fowler, M. Zhao, *J. Cleaner Prod.* **2020**, *247*, 119115.

[10] K.-H. Nam, K. H. Chae, J.-H. Choi, K.-J. Jeon, C.-M. Park, *Chem. Eng. J.* **2021**, *417*, 129242.

[11] J. H. Kim, S. Kim, J. H. Han, S. B. Seo, Y. R. Choi, J. Lim, Y. A. Kim, *Carbon Lett.* **2023**, *33*, 325–333.

[12] J. P. Sullivan, A. Bose, *Electrochem. Commun.* **2022**, *141*, 107353.

[13] Y. Son, N. Kim, T. Lee, Y. Lee, J. Ma, S. Chae, J. Sung, H. Cha, Y. Yoo, J. Cho, *Adv. Mater.* **2020**, *32*, 2003286.

[14] S. Chae, M. Ko, K. Kim, K. Ahn, J. Cho, *Joule* **2017**, *1*, 47–60.

[15] L. Sun, Y. Liu, R. Shao, J. Wu, R. Jiang, Z. Jin, *Energy Storage Mater.* **2022**, *46*, 482–502.

[16] S. He, S. Huang, S. Wang, I. Mizota, X. Liu, X. Hou, *Energy Fuels* **2020**, *35*, 944–964.

[17] M. Ge, C. Cao, G. M. Biesold, C. D. Sewell, S. M. Hao, J. Huang, W. Zhang, Y. Lai, Z. Lin, *Adv. Mater.* **2021**, *33*, 2004577.

[18] Y. Jin, B. Zhu, Z. Lu, N. Liu, J. Zhu, *Adv. Energy Mater.* **2017**, *7*, 1700715.

[19] W. Luo, Y. Wang, S. Chou, Y. Xu, W. Li, B. Kong, S. X. Dou, H. K. Liu, J. Yang, *Nano Energy* **2016**, *27*, 255–264.

[20] S. Chae, S. H. Choi, N. Kim, J. Sung, J. Cho, *Angew. Chem. Int. Ed.* **2020**, *59*, 110–135.

[21] M. N. Obrovac, V. L. Chevrier, *Chem. Rev.* **2014**, *114*, 11444–11502.

[22] Y. Xu, Y. Zhu, Y. Liu, C. Wang, *Adv. Energy Mater.* **2013**, *3*, 128–133.

[23] H. Ying, W. Q. Han, *Adv. Sci.* **2017**, *4*, 1700298.

[24] M. Zhang, T. Wang, G. Cao, *Int. Mater. Rev.* **2015**, *60*, 330–352.

[25] W.-J. Zhang, *J. Power Sources* **2011**, *196*, 13–24.

[26] W. Li, X. Sun, Y. Yu, *Small Methods* **2017**, *1*, 1600037.

[27] G. Ma, W. Yang, C. Xu, S. Che, Y. Li, H. Liu, N. Chen, G. Zhang, H. Liu, N. Wu, Y. Wang, Y. Li, *Electrochim. Acta* **2022**, *428*, 140898.

[28] X. Chang, T. Wang, Z. Liu, X. Zheng, J. Zheng, X. Li, *Nano Res.* **2017**, *10*, 1950–1958.

[29] H. Yang, B. Wang, Y. Li, H. Du, J. Zhao, Y. Xie, *J. Alloys Compd.* **2023**, *945*, 169302.

[30] R. Li, S. Nie, C. Miao, Y. Xin, H. Mou, G. Xu, W. Xiao, *J. Colloid Interface Sci.* **2022**, *606*, 1042–1054.

[31] W.-L. Li, H. Lai, C.-H. Sun, Y.-Y. Lin, Y.-H. Sun, J.-M. Nan, *J. Alloys Compd.* **2023**, *948*, 169811.

[32] Z. Zhu, S. Wang, J. Du, Q. Jin, T. Zhang, F. Cheng, J. Chen, *Nano Lett.* **2014**, *14*, 153–157.

[33] J. Yang, M. Winter, J. Besenhard, *Solid State Ionics* **1996**, *90*, 281–287.

[34] Y. Xu, Q. Liu, Y. Zhu, Y. Liu, A. Langrock, M. R. Zachariah, C. Wang, *Nano Lett.* **2013**, *13*, 470–474.

[35] Y. Liu, N. Zhang, L. Jiao, J. Chen, *Adv. Mater.* **2015**, *27*, 6702–6707.

[36] J. Liu, D. Zhang, J. Cui, P. Li, X. Xu, Z. Liu, J. Liu, C. Peng, D. Xue, M. Zhu, J. Liu, *Small* **2023**, *19*, 2301444.

[37] X. Xu, Z. Wang, D. Zhang, S. Zuo, J. Liu, M. Zhu, *ACS Appl. Mater. Interfaces* **2020**, *12*, 51478–51487.

[38] O. Li, J. Kang, J. Urashima, N. Saito, *Int. J. Plasma Environ. Sci. Technol.* **2013**, *7*, 31–36.

[39] W. Tian, H. Zhang, X. Duan, H. Sun, G. Shao, S. Wang, *Adv. Funct. Mater.* **2020**, *30*, 1909265.

[40] Y. Li, J.-G. Wang, W. Hua, H. Liu, B. Wei, *J. Mater. Chem. A* **2019**, *7*, 16883–16891.

[41] H.-S. Yang, M.-W. Park, K.-H. Kim, O. L. Li, T.-I. Jeon, J. Kang, *Carbon* **2022**, *189*, 251–264.

[42] H. Kim, D.-Y. Kim, S. Zen, J. Kang, N. Takeuchi, *ACS Appl. Mater. Interfaces* **2020**, *12*, 43750–43760.

[43] J. Hu, S. Zhong, T. Yan, *J. Power Sources* **2021**, *508*, 230342.

[44] H. Kim, H. Yang, J. Kang, N. Takeuchi, *Carbon* **2021**, *182*, 242–253.

[45] X. Huang, S. Cui, J. Chang, P. B. Hallac, C. R. Fell, Y. Luo, B. Metz, J. Jiang, P. T. Hurley, J. Chen, *Angew. Chem. Int. Ed.* **2015**, *54*, 1490–1493.

[46] Y. Feng, K. Wu, H. Dong, X. Huang, C. Bai, J. Ke, D. Xiong, M. He, *Colloids Surf. A* **2020**, *602*, 125069.

[47] Z. Xu, L. Fan, X. Ni, J. Han, R. Guo, *RSC Adv.* **2019**, *9*, 8753–8758.

[48] S.-C. Wu, C.-W. Lin, P.-C. Chang, T.-Y. Yang, S.-Y. Tang, D.-C. Wu, C.-R. Liao, Y.-C. Wang, L. Lee, Y.-J. Yu, Y.-L. Chueh, *ACS Appl. Mater. Interfaces* **2023**, *15*, 15279–15289.

[49] K.-Y. Zhang, Y.-Q. Fu, H.-H. Liu, J.-L. Yang, M.-Y. Su, Y. Wang, X.-L. Wu, *Phys. Scr.* **2023**, *98*, 125977.

[50] K. H. Chen, V. Goel, M. J. Namkoong, M. Wied, S. Müller, V. Wood, J. Sakamoto, K. Thornton, N. P. Dasgupta, *Adv. Energy Mater.* **2021**, *11*, 2003336.

[51] L. Xie, C. Tang, Z. Bi, M. Song, Y. Fan, C. Yan, X. Li, F. Su, Q. Zhang, C. Chen, *Adv. Energy Mater.* **2021**, *11*, 2101650.

[52] B. Qin, W. Mang, S. Wu, Y. Li, C. Liu, Y. Zhang, H. Fan, *Chin. Chem. Lett.* **2023**, 108921.

[53] X.-T. Wang, X. Yang, J.-Z. Guo, Z.-Y. Gu, E. H. Ang, Z.-H. Sun, W.-H. Li, H.-J. Liang, X.-L. Wu, *J. Mater. Sci. Technol.* **2022**, *102*, 72–79.

[54] J. Z. Guo, H. X. Zhang, Z. Y. Gu, M. Du, H. Y. Lü, X. X. Zhao, J. L. Yang, W. H. Li, S. Kang, W. Zou, X. L. Wu, *Adv. Funct. Mater.* **2022**, *32*, 2209482.

[55] X. X. Zhao, W. Fu, H. X. Zhang, J. Z. Guo, Z. Y. Gu, X. T. Wang, J. L. Yang, H. Y. Lü, X. L. Wu, E. H. Ang, *Adv. Sci.* **2023**, *10*, 2301308.

[56] H. Zhang, L. Wang, H. Li, X. He, *ACS Energy Lett.* **2021**, *6*, 3719–3724.

[57] Y. Xiao, Y. Mao, T. Li, X. Hao, W. Wang, *ACS Appl. Mater.* **2023**, *15*, 45938–45948.

[58] J. Kang, H. V. Kim, S. A. Chae, K. H. Kim, *Small* **2018**, *14*, 1704394.

[59] J.-L. Wei, Z.-Y. Wang, Y.-H. Sun, G.-L. Zhang, D.-C. Guan, J.-M. Nan, *Electrochim. Acta* **2021**, *375*, 138026.